Bionanofiber Assisted Decoration of Few-Layered $MoSe_2$ Nanosheets on 3D Conductive Networks for Efficient Hydrogen Evolution

Feili Lai, Dingyu Yong, Xueliang Ning, Bicai Pan, Yue-E Miao, and Tianxi Liu**

***M**olybdenum diselenide ($MoSe_2$) has emerged as a promising electrocatalyst for hydrogen evolution reaction (HER). However, its properties are still confined due to the limited active sites and poor conductivity. Thus, it remains a great challenge to synergistically achieve structural and electronic modulations for $MoSe_2$-based HER catalysts because of the contradictory relationship between these two characteristics. Herein, bacterial cellulose-derived carbon nanofibers are used to assist the uniform growth of few-layered $MoSe_2$ nanosheets, which effectively increase the active sites of $MoSe_2$ for hydrogen atom adsorption. Meanwhile, carbonized bacterial cellulose (CBC) nanofibers provide a 3D network for electrolyte penetration into the inner space and accelerate electron transfer as well, thus leading to the dramatically increased HER activity. In acidic media, the CBC/$MoSe_2$ hybrid catalyst exhibits fast hydrogen evolution kinetics with onset overpotential of 91 mV and Tafel slope of 55 mV dec^{-1}, which is much more outstanding than both bulk $MoSe_2$ aggregates and CBC nanofibers. Furthermore, the fast HER kinetics are well supported by theoretical calculations of density-functional-theory analysis with a low activation barrier of 0.08 eV for H_2 generation. Hence, this work highlights an efficient solution to develop high-performance HER catalysts by incorporating biotemplate materials, to simultaneously achieve increased active sites and conductivity.*

F. L. Lai, Prof. T. X. Liu
State Key Laboratory of Molecular Engineering of Polymers
Department of Macromolecular Science
Fudan University
Shanghai 200433, P. R. China
E-mail: txliu@dhu.edu.cn

F. L. Lai, D. Y. Yong, Prof. B. C. Pan
Hefei National Laboratory for Physical Science at Microscale
Collaborative Innovation Center of Chemistry for Energy Materials
University of Science and Technology of China
Hefei 230026, P. R. China

X. L. Ning, Dr. Y. E. Miao, Prof. T. X. Liu
State Key Laboratory for Modification of Chemical Fibers and Polymer Materials
College of Materials Science and Engineering
Donghua University
Shanghai 201620, P. R. China
E-mail: yuee_miao@dhu.edu.cn

DOI: 10.1002/smll.201602866

1. Introduction

Electrocatalytic hydrogen evolution reaction (HER) has been considered as a promising solution to meet the growing demand for energy and environmental concerns caused by the severe consumption of traditional fossil fuels.[1,2] Noble metals, especially platinum, are well known to be one kind of the most effective catalysts for HER,[3,4] while they are still severely hindered for wide-spread utilization due to the high cost and elemental scarcity. Therefore, it is of essential necessity to develop earth-abundant HER electrocatalysts for economic and competitive hydrogen production. Over the past decades, transition metal dichalcogenides (TMDs), such as MoS_2, TiS_2, WS_2, and WSe_2, have received tremendous attention and been regarded as promising alternatives for noble metals due to their high activity and outstanding stability.[5–8] As a typical TMD semiconducting material, molybdenum diselenide ($MoSe_2$) is vertically stacked by sandwiched Se–Mo–Se layers with weak van der Waals interactions.[9–11] The theoretical calculation reveals that $MoSe_2$ possesses

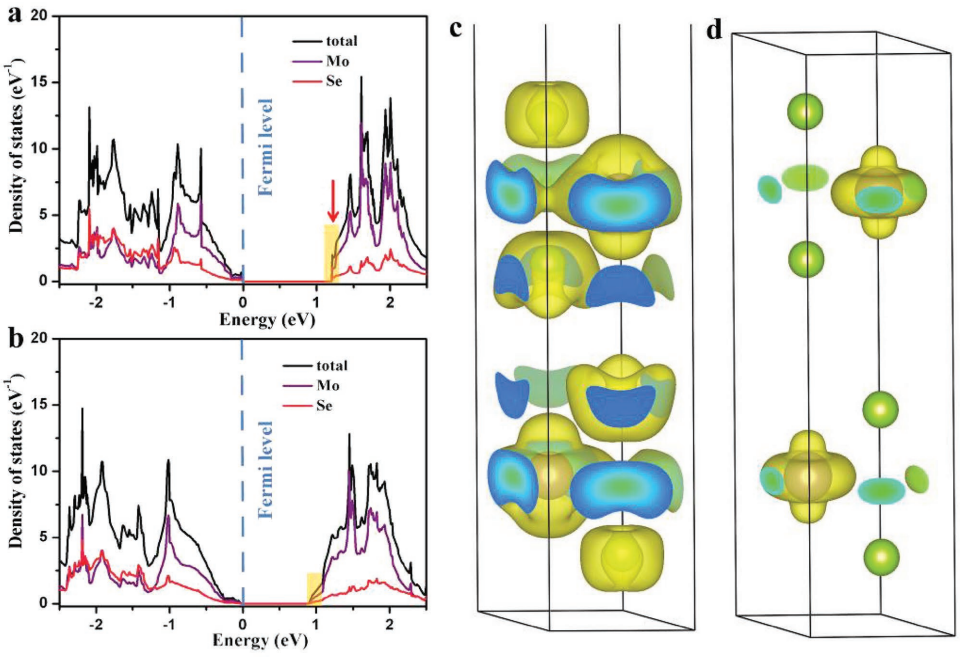

Figure 1. DFT calculations. Calculated DOS for a) double-layered $MoSe_2$ and b) bulk $MoSe_2$. The shadowed region highlights the increased state density at the conduction band edge of double-layered $MoSe_2$. Charge density distribution for the conduction band edge of c) double-layered $MoSe_2$ and d) bulk $MoSe_2$.

lower Gibbs free energy than MoS_2 for hydrogen adsorption onto the active edges, which is because of the more metallic nature of $MoSe_2$,[12,13] indicating its more outstanding HER performance as an alternative of MoS_2-based catalysts.[14–16] However, confined by the scarce catalytically active sites, bulk $MoSe_2$ is still a poor HER catalyst.[17] Therefore, it is desirable and imperative to develop high-performance $MoSe_2$-based HER electrocatalysts by constructing feasible nanostructures to effectively increase their exposed active edges. Herein, few-layered $MoSe_2$ nanosheets are considered as an outstanding platform to promote the hydrogen generation ability by affording abundant catalytically active sites. More importantly, according to the density-functional-theory (DFT) calculations,[18,19] we have revealed that $MoSe_2$ possesses an increased density of states (DOS) at the conduction band edge as compared to its bulk counterpart once the thickness is down to few atomic layers, as shown in **Figure 1**a,b by taking double-layered $MoSe_2$ as an example. Meanwhile, as the spatial distribution of charge density near the Fermi level (Figure 1c,d; Figure S1 in the Supporting Information) is divulged, most of the charge density concentrates on the surface of double-layered $MoSe_2$, demonstrating that more active electrons can be generated on the exposed surfaces of few-layered $MoSe_2$ nanosheets than bulk $MoSe_2$. Therefore, the electric-excited electrons are easier to gather on the surface to react with adsorbed hydrogen atoms, resulting in enhanced hydrogen evolution reaction.

Inspired by the aforementioned concepts, the rational synthesis of few-layered $MoSe_2$ nanosheets is of great importance. Up to now, a wide range of methods have been developed for the fabrication of few-layered $MoSe_2$ nanosheets, such as chemical vapor deposition, liquid-phase exfoliation, and wet chemical synthesis, among which wet chemical synthesis is regarded as one of the most promising solutions for industrial production due to its facile process and high yield.[20–22] Using wet chemical synthesis approach, for example, macroporous $MoSe_2$ films,[23] hierarchical and ultrathin Mo-rich $MoSe_{2-x}$ nanosheets,[9] and porous $MoSe_2$ nanosheets,[24] have been developed as high-performance HER catalysts. Although few-layered $MoSe_2$ nanosheets have been reported to possess more exposed active sites than their bulk ones, the intrinsic poor conductivity resulting from the large bandgap of $MoSe_2$ still severely limits their overall HER rate.[25] Therefore, the simultaneous optimization of both active sites and conductivity still remains a great challenge for $MoSe_2$ nanosheets because of the contradictory relationship between these two characteristics. To overcome this obstacle, enormous efforts have been made to pursue a reasonable route, which can not only enhance the conductivity of $MoSe_2$ nanosheets but also keep the active sites as well. Satisfyingly, carbon-based materials, with excellent conductivity, extremely large surface area, and structural stability, have become promising candidates to lower the bandgaps of metal-based materials by modulating their electronic state.[13,26,27] As a novel bionanofiber precursor for carbon materials, bacterial cellulose (BC), with the formula of $(C_6H_{10}O_5)_n$, is a polysaccharide normally produced via the microbial fermentation by using certain types of bacteria.[28–30] With the competitive superiorities of high crystallinity, free of lignin/semicellulose, abundant resource, and eco-friendliness, bacterial cellulose has been an emerging nanomaterial in the particular fields of energy conversion and storage.[31,32]

Herein, bacterial cellulose is chosen as the carbon precursor to support the growth of $MoSe_2$ nanosheets, leading to carbonized bacterial cellulose (CBC)/$MoSe_2$ hybrid with

hierarchical structure as potential HER catalyst. As expected, $MoSe_2$ nanosheets are uniformly anchored on the surface of CBC nanofibers to form a unique core–shell structure which is attributed to the as-formed 3D network of bacterial cellulose-derived carbon nanofibers. Meanwhile, due to the assistance of CBC template, $MoSe_2$ nanosheets exhibit few-layered characteristic instead of bulk aggregates, which dramatically increase the active sites of CBC/$MoSe_2$ hybrid. Benefiting from the synergistic structural and electronic modulations, CBC/$MoSe_2$ hybrid catalyst displays an optimal HER activity with an onset overpotential of 91 mV and Tafel slope of 55 mV dec^{-1}, as well as excellent cycling stability. Hence, this work provides a simple but effective pathway to simultaneously enhance the active sites and conductivity of $MoSe_2$-based HER catalysts by incorporating biomaterial nanofiber template.

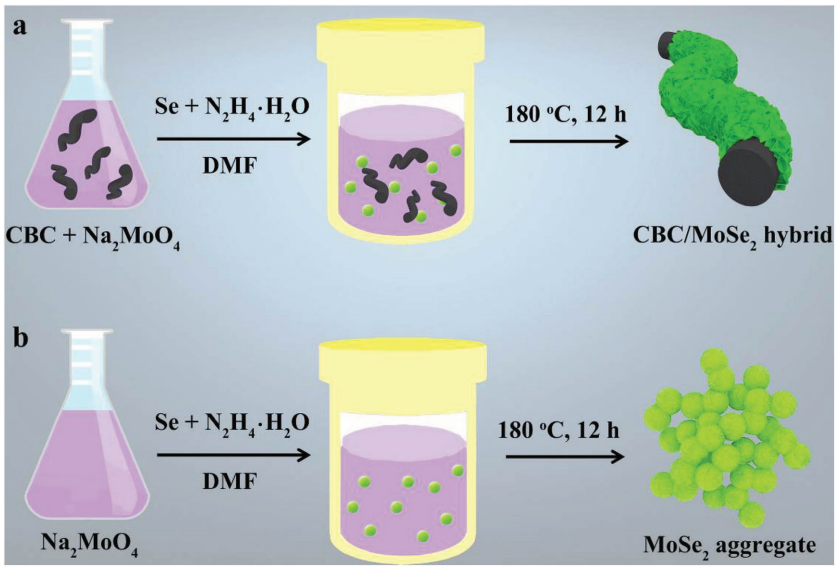

Figure 2. Schematic illustration of the preparation of a) CBC/$MoSe_2$ hybrid with CBC nanofiber as template and b) $MoSe_2$ aggregates without CBC nanofiber template.

2. Results and Discussion

The fabrication process of CBC/$MoSe_2$ hybrid is displayed in **Figure 2**a. Representative field emission scanning electron microscope (FESEM) and transmission electron microscopy (TEM) images of CBC nanofibers (**Figure 3**a; Figure S2 in the Supporting Information) reveal a 3D network consisting of numerous individual carbon nanofibers with average diameter of 30–60 nm and length of a few micrometers. Due to the huge aspect ratio of CBC nanofibers, the formed 3D network possesses porous structure for the penetration of $MoSe_2$ precursor, thus being an ideal template for anchoring of $MoSe_2$ nanoparticles. Before the in situ solvothermal growth of $MoSe_2$, CBC nanofibers are acid-treated to introduce functional groups, such as hydroxyl and carboxyl groups, thus achieving their good dispersion. Consequently, $MoSe_2$ nanosheets are uniformly and densely grown on the skeleton of CBC nanofibers, with the complete retention of 3D interconnected and porous networks (Figure 3b,c). The obtained CBC/$MoSe_2$ hybrid possesses an increased diameter of about 150 nm due to the anchoring of $MoSe_2$ nanosheets. With the assistance of CBC template, $MoSe_2$ nanosheets are decorated throughout the longitudinal axis, which reasonably promotes the exposure of active sites for few-layered $MoSe_2$ nanosheets (Figure 3d). From the top-view high-resolution TEM (HR-TEM) image in Figure 3e, five to eight single layers with an interplanar spacing of 6.2 Å can be observed for an individual $MoSe_2$ nanosheet, which matches well with the (002) lattice spacing of $MoSe_2$. Meanwhile, bulk $MoSe_2$ aggregates obtained under identical synthesis conditions (Figure 2b) display "ball-like" morphology (Figure 3f; Figure S3 in the Supporting Information), which definitely hinder the electrolyte penetration into the inner space, as well as the electron transfer outward the surface of bulk $MoSe_2$. Hence, the CBC/$MoSe_2$ hybrid structure demonstrates that CBC nanofibers are outstanding support to mediate the growth of $MoSe_2$ nanosheets, which are beneficial to not only releasing the few-layered characteristic of $MoSe_2$ nanosheets with increased active sites, but also overcoming the poor intrinsic conductivity of bulk $MoSe_2$.

As shown in the X-ray diffraction (XRD) patterns (**Figure 4**a), both the bulk $MoSe_2$ aggregates and CBC/$MoSe_2$ hybrid display four diffraction peaks at 2θ = 13.2°, 31.9°, 38.1°, and 56.2°, corresponding to (002), (100), (103), and (110) planes of hexagonal $MoSe_2$ (JCPDS 87-2419), respectively, proving the successful preparation of $MoSe_2$ nanocrystals.[33] In addition, a broad peak ranging from 2θ = 20° to 30° observed in the XRD pattern of CBC/$MoSe_2$ hybrid is ascribed to the amorphous CBC nanofibers (JCPDS 01-0646), indicating the coexistence of $MoSe_2$ and CBC nanofibers in the hybrid materials. X-ray photoelectron spectra (XPS) measurements were also carried out to analyze the chemical composition and state of the CBC/$MoSe_2$ hybrid. In the survey spectrum (Figure 4b), characteristic peaks for C, Mo, Se, and O appear as the principal elemental components, demonstrating no detectable impurities for CBC/$MoSe_2$ hybrid. As for the high-resolution spectrum of Mo 3d in Figure 4c, two characteristic peaks located at 229.1 and 232.2 eV are observed from Mo $3d_{5/2}$ and Mo $3d_{3/2}$ orbitals, suggesting the dominance of $Mo^{(IV)}$ in the product.[26] Meanwhile, the Se 3d region with a single doublet of $3d_{5/2}$ peak at 54.6 eV and $3d_{3/2}$ peak at 55.4 eV (Figure 4d), as well as Se 3p region of $3p_{3/2}$ at 161.1 eV and $3p_{1/2}$ at 166.7 eV (Figure 4e) respectively, is consistent with the –2 oxidation state of selenium. Moreover, the detailed compositional analysis reveals that the surface atomic ratio of Se:Mo is approximately to be 2.2:1, giving the direct evidence to the formula of $MoSe_2$.

As verified by DFT calculations, the few-layered $MoSe_2$ nanosheets with nanocrystalline structure could efficiently enhance the exposure of electrochemically active sites of

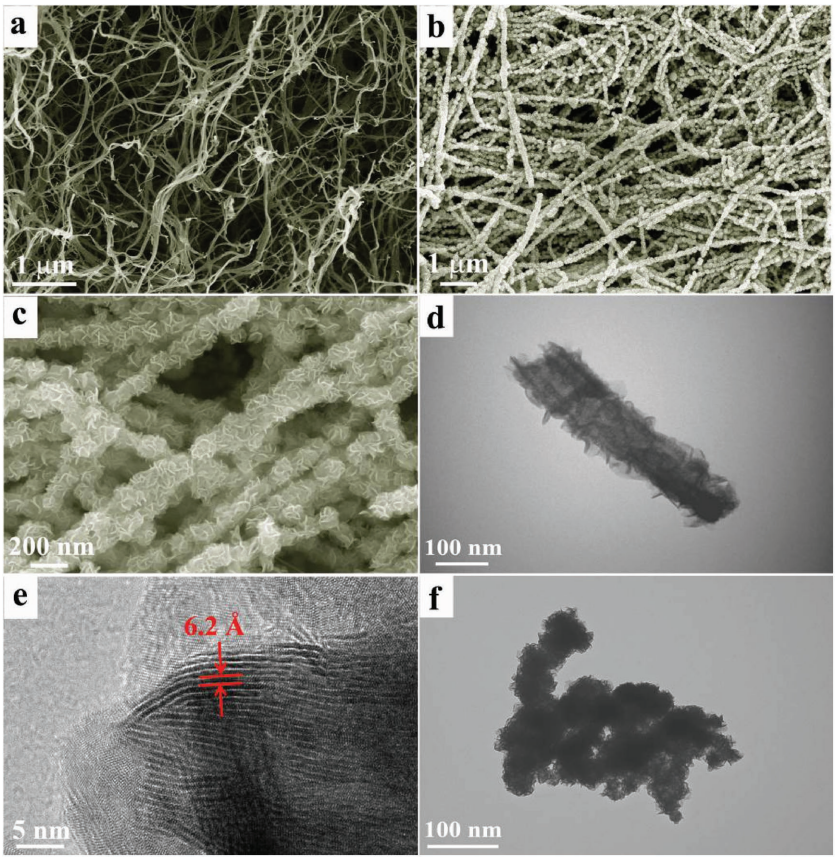

Figure 3. a) SEM image of CBC nanofibers. b,c) SEM images, d) TEM image and e) HR-TEM image of CBC/$MoSe_2$-2 hybrid. f) TEM image of bulk $MoSe_2$ aggregates without carbonized bacterial cellulose nanofibers as template during the solvothermal synthesis.

$MoSe_2$ layers, leading to optimized electrocatalytic abilities. Additionally, the CBC nanofiber skeleton improves the electrical conductivity of integrated CBC/$MoSe_2$ hybrid, which is beneficial to promoting the electron transfer rate for better electron exchange processes. In order to verify our expectation, electrochemical measurements of different CBC/$MoSe_2$ hybrids, as well as the bulk $MoSe_2$ aggregates and CBC nanofibers were performed as HER electrocatalysts. All of the experiments were carried out within 0.5 M H_2SO_4 solution using a three-electrode setup with the same loading of 0.285 mg cm^{-2} on a glassy carbon electrode. As displayed in **Figure 5**a, all of the CBC/$MoSe_2$ hybrids possess much lower onset overpotentials (η) than the bulk $MoSe_2$ aggregates, suggesting the simultaneous enhancement of active sites and conductivity of the hybrids derived from few-layered $MoSe_2$ nanosheets and CBC nanofiber template. Particularly, the CBC/$MoSe_2$-2 hybrid exhibits the lowest value of 91 mV (**Table 1**) which is much more superior over the previously reported $MoSe_x$-based catalysts (Table S1, Supporting Information),[9,26,34–41] while inferior performances of 160 and 123 mV are observed for CBC/$MoSe_2$-1 and CBC/$MoSe_2$-3 hybrids, respectively. Notably, the morphologies of CBC/$MoSe_2$-1 and CBC/$MoSe_2$-3 hybrids play a key role as shown in Figure S5 in the Supporting Information. The sparse growth of $MoSe_2$ nanosheets for CBC/$MoSe_2$-1 hybrid (Figure S5a in the Supporting Information) results in scarce active sites toward H atom adsorption while the excessive decoration of $MoSe_2$ aggregates for CBC/$MoSe_2$-3 hybrid (Figure S5b in the Supporting Information) leads to poor conductivity and restricted electron transfer. Moreover, the cathodic current density is also regarded as an important evaluation criterion for HER performance. As displayed in Figure 5a, the CBC/$MoSe_2$-2 hybrid possesses the largest cathodic current density among all of the tested samples, with 87 mA cm^{-2} at the overpotential of 300 mV, which is 15 and 174 times higher than those of bulk $MoSe_2$ aggregates and CBC nanofibers respectively, indicating its prominent hydrogen evolution behavior. To obtain further insight into the CBC/$MoSe_2$ hybrids, Tafel plots of various samples were investigated (Figure 5b). The corresponding Tafel plots demonstrate that the CBC/$MoSe_2$ hybrids possess smaller Tafel slope than both of single-component CBC nanofiber (112 mV dec^{-1}) and bulk $MoSe_2$ aggregate (105 mV dec^{-1}). Furthermore, the as-obtained CBC/$MoSe_2$-2 hybrid displays the lowest Tafel slope of 55 mV dec^{-1}, leading to a faster increment of HER rate, which implies its potential applications.

To prove the enhanced conductivity of CBC/$MoSe_2$ hybrid under HER process, electrochemical impedance spectroscopy (EIS) tests were conducted as shown in Figure 5c. An apparent decrease of the charge-transfer resistance can be observed for CBC/$MoSe_2$ hybrid compared with that of bulk $MoSe_2$ aggregates, due to the 3D network and larger surface area for faster interdomain electron transport. Meanwhile, the smaller solution resistance of the CBC/$MoSe_2$ hybrid with respect to bulk $MoSe_2$ aggregates demonstrates the positive role of the highly conductive CBC nanofibers to generate uniformly anchored few-layered $MoSe_2$ nanosheets and provide efficient pathways for rapid electron transfer as well. Consequently, the CBC/$MoSe_2$ hybrid achieves an integrated structure with both highly exposed active sites and increased overall conductivity, leading to its superior HER activity.

Stability is another significant criterion to evaluate the HER activity of a catalyst. To investigate the durability of CBC/$MoSe_2$ hybrid in an acidic environment, continuous cyclic voltammetry between –0.4 and 0.2 V versus RHE was conducted for 1000 cycles with a scan rate of 100 mV s^{-1}. Negligible difference can be observed from the linear sweep voltammetry curves before and after 1000 cycles, with low onset potentials and slight decay in the current densities (Figure 5d), confirming that CBC/$MoSe_2$ hybrid is a highly stable catalyst to withstand accelerated degradation. Furthermore, the practical operation of CBC/$MoSe_2$ hybrid was examined under a fixed overpotential of 200 mV, resulting in a continuous generation of gaseous hydrogen. As displayed in Figure S6 in the Supporting Information, the

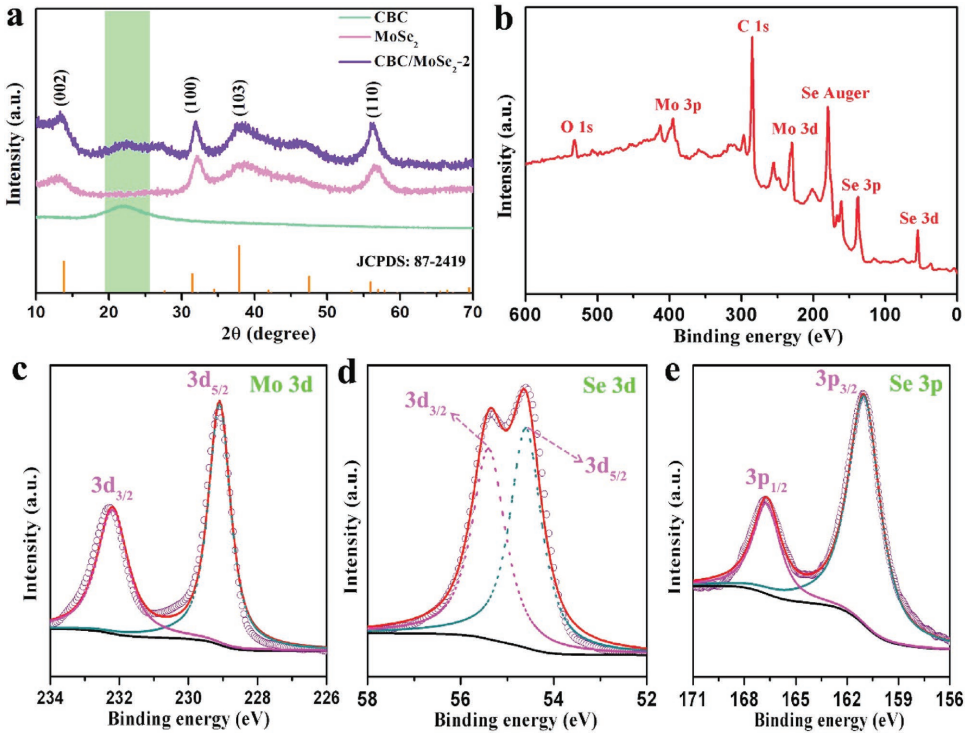

Figure 4. a) XRD patterns of CBC nanofibers, bulk $MoSe_2$ aggregates, and the CBC/$MoSe_2$-2 hybrid. XPS spectra of CBC/$MoSe_2$-2 hybrid: b) survey spectrum, c) Mo 3d, d) Se 3d, and e) Se 3p.

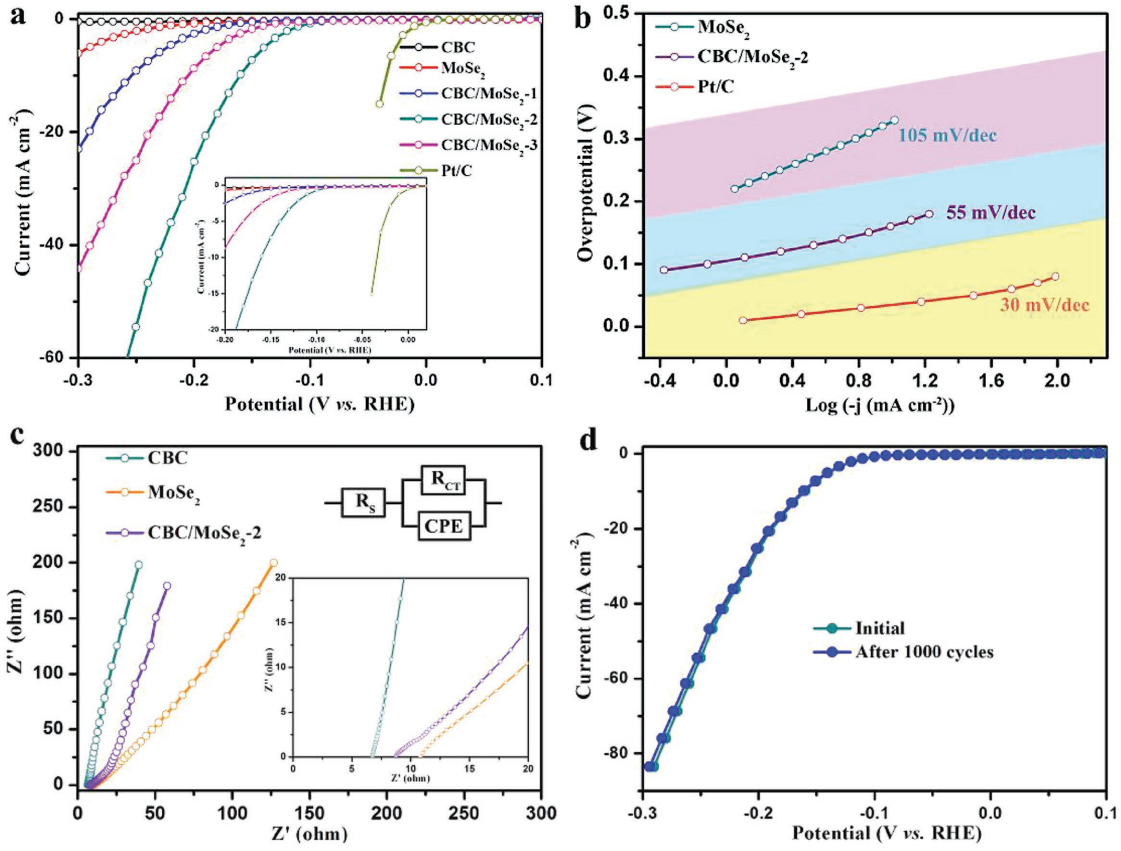

Figure 5. a) Polarization curves and b) the corresponding Tafel plots of various CBC/$MoSe_2$ hybrids, $MoSe_2$ aggregates, and Pt/C. Inset: the enlargement of the region near the onset potential. c) Nyquist plots of CBC/$MoSe_2$-2 hybrid, $MoSe_2$ aggregates, and CBC nanofibers. The fitted curves are presented by solid lines. Inset: the expanded high-frequency region of the plots. d) Durability test for CBC/$MoSe_2$-2 hybrid before and after 1000 cycles.

Table 1. Comparison of catalytic parameters of different HER materials.

Materials	Onset potential [mV vs RHE]	Tafel slope [mV dec^{-1}]	$j^{a)}$ [mA cm^{-2}]
CBC	402	112	0.2
$MoSe_2$	203	105	6
CBC/$MoSe_2$-1	160	71	23
CBC/$MoSe_2$-2	91	55	87
CBC/$MoSe_2$-3	123	63	44
Pt/C	0	30	–

[a)]Cathodic current densities (j) were recorded at η = 300 mV.

current density remains stable at about 26 mA cm^{-2} for electrolysis over 9000 s with only a slight degradation, which might be caused by the accumulation of H_2 bubbles on the electrode surface that hinders the reaction.[6] Therefore, this exceptional durability demonstrates the promising practical applications of CBC/$MoSe_2$ hybrid over the long term.

To further understand the catalytic efficacy arising from the incorporation of CBC template, the detailed HER pathway for CBC/$MoSe_2$ hybrid was investigated by DFT calculations. In general, ΔG_H is regarded as a key descriptor in the theoretical prediction of HER activity on various solid electrodes. According to Sabatier principle, $\Delta G_H \approx 0$ is beneficial to achieving a maximum rate for the overall hydrogen evolution reaction. From the physical chemistry perspective, a good HER catalyst should form a sufficiently strong bond with adsorbed hydrogen atoms, that is low ΔG_H, to facilitate the electrochemical process, while it should be weak enough with high ΔG_H to assure a facile bond breaking for further releasing of gaseous H_2 product as well.[42] Hence, it provides a feasible method to discover potential catalysts with optimum HER activities by adjusting the value of ΔG_H to ≈0. To be an analog compound of $MoSe_2$, the hydrogen adsorption free-energy calculations reveal that Mo-edges of MoS_2 exhibit a strong adhesion to the carbon support which can weaken the hydrogen binding and optimize the ΔG_H of MoS_2/carbon hybrids,[42] demonstrating similar superiority of the interfaces between CBC nanofibers and $MoSe_2$ nanosheets in this work. As shown in **Figure 6**a,b, there are three aspects leading to the superior HER activity of CBC/$MoSe_2$ hybrid: (1) The 3D network of carbonized bacterial cellulose nanofibers provides a porous skeleton, which is beneficial for the penetration of electrolyte into the inner space. (2) The high conductivity of carbon support makes it easier for electron transfer compared with bulk $MoSe_2$ aggregates. (3) Few-layered $MoSe_2$ nanosheets generated by incorporating bionanofiber template create a great deal of active sites for H atoms adsorption and HER reaction.

For the HER reaction in acidic media, three principle steps have been proposed to convert H^+ into H_2, commonly referred to as the Volmer, Heyrovsky, and Tafel reactions[43]

$$H_3O^+ + e^- \rightarrow H_{ads} + H_2O \,(b \approx 120 \text{ mV dec}^{-1}) \quad (1)$$

$$H_{ads} + H_3O^+ + e^- \rightarrow H_2 + H_2O \,(b \approx 40 \text{ mV dec}^{-1}) \quad (2)$$

$$H_{ads} + H_{ads} \rightarrow H_2 \,(b \approx 30 \text{ mV dec}^{-1}) \quad (3)$$

For a complete HER process, two separate pathways (the Volmer–Tafel or the Volmer–Heyrovsky mechanism) should be involved to produce molecular H_2. Although the HER mechanism for $MoSe_2$-based catalysts still remains inconclusive due to the reaction complexity, the Tafel slope of CBC/$MoSe_2$ hybrid in this work (Figure 5b) is 55 mV dec^{-1}, which demonstrates its Volmer–Heyrovsky mechanism during the electrochemical reactions. Furthermore, the detailed HER pathway on CBC/$MoSe_2$ hybrid catalyst was investigated by DFT calculations (Figure 6c). In the DFT calculation, one H atom is first adsorbed on the active site of Se atom,

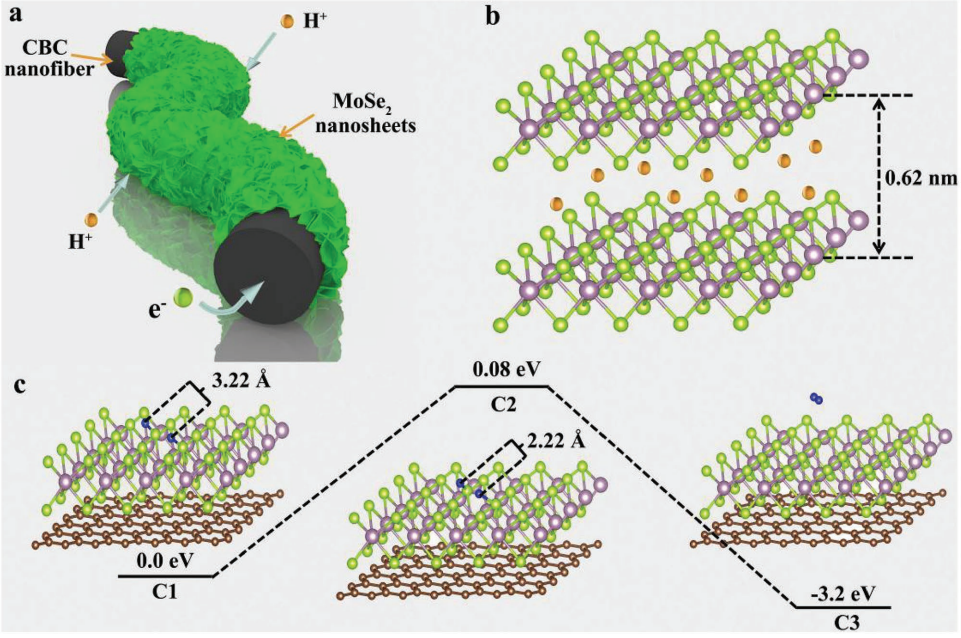

Figure 6. a,b) Illustration of the electron and ion transport pathways in CBC/$MoSe_2$ hybrid. c) Schematic reaction pathway of HER process for CBC/$MoSe_2$ hybrid (green, purple, blue, and brown balls indicate Se, Mo, H atom/H^+, and C, respectively).

while another H^+ gets close to the adsorbed H atom with H–H distance of 3.22 Å (Figure 6C1). After migrating to a proper condition, the two approached H atoms on the edge of Se atoms form a transition state with H–H distance of 2.22 Å (Figure 6C2). Finally, the adsorbed H_2 makes its way to desorption (Figure 6C3). The calculated activation barrier for generation of H_2 is 0.08 eV, which is even lower than the energy for H atomic migration, including path-ab of 0.13 eV and path-ac of 0.21 eV (Figure S7 in the Supporting Information). Hence, the calculated low energy agrees well with the aforementioned experimental HER kinetics, indicating the great practical values of CBC/$MoSe_2$ hybrid catalyst.

3. Conclusion

In summary, 3D CBC/$MoSe_2$ hybrid was prepared via the combination of high-temperature carbonization and hydrothermal reaction. The active sites and conductivity play key roles during the hydrogen evolution reaction process, while it still remains a great challenge to simultaneously optimize these two parameters. Interestingly, the CBC nanofibers are found to effectively overcome this problem by inducing the controllable growth of few-layered $MoSe_2$ nanosheets to expose more active sites, and providing 3D conductive network for enhancing electron transfer at the same time. As expected, the obtained CBC/$MoSe_2$ hybrid catalyst exhibits high activity for hydrogen evolution with onset overpotential of 91 mV and Tafel slope of 55 mV dec^{-1}, which can be ascribed to the synergistic effect between few-layered $MoSe_2$ nanosheets and carbonized bacterial cellulose nanofibers. Furthermore, the mechanism for HER process is investigated via density-functional-theory calculations, which theoretically proves the low activation barrier of 0.08 eV for hydrogen evolution. Hence, this work will broaden the vision to enhance the activity of various metal-based electrocatalysts by incorporating biomaterial-derived templates to synergistically modulate the exposed active sites as well as conductivity.

4. Experimental Section

Materials: The bacterial cellulose pellicles (30 × 40 cm^2) were obtained from Hainan Yide Food Co. Ltd. Selenium powder (Se, 99.99%), sodium molybdate (Na_2MoO_4, 99.99%), and hydrazine hydrate ($N_2H_4{\cdot}H_2O$, 50 wt% in water) were provided by Sinopharm Chemical Reagent Co. Ltd. *N,N*-dimethylformamide (DMF) and ethanol were purchased from Shanghai Chemical Reagent Company. Pt/C catalyst (20 wt% platinum on carbon black) was obtained from Alfa Aesar. All chemicals were of analytic grade and used as received.

Synthesis of CBC/$MoSe_2$ Hybrids: First, carbonized bacterial cellulose nanofibers were prepared according to the previous method.[44] Briefly, BC pellicles were soaked in 0.1 M NaOH solution for 6 h, and then washed with deionized water for several times to pH ≈ 7. Subsequently, the hydrous BC pellicles were frozen by liquid nitrogen and freeze-dried to obtain dried BC pellicles. Then, the dried BC pellicles were heated up to 800 °C in N_2 atmosphere with a heating rate of 5 °C min^{-1} and maintained for 1 h to obtain CBC nanofibers.

As for the solvothermal process, 3 mg mL^{-1} of Se solution was firstly prepared by using hydrazine hydrate as the solvent. To prepare CBC/$MoSe_2$ hybrid, 10 mg of acid-treated CBC nanofibers and 4.6 mg of Na_2MoO_4 were dispersed in 10 mL DMF under sonication for at least 20 min. Then, 1 mL of Se solution was dropped into the above solution under vigorous stirring to form a homogeneous suspension with Mo:Se molar ratio of 1:2. After being stirred for 30 min, the mixed solution was transferred into a Teflon-line autoclave and maintained at 180 °C for 12 h. Then, the obtained products were collected by centrifugation, washed with deionized water and ethanol for several times, and dried at 60 °C under vacuum. After dried overnight, the products were annealed in N_2 at 450 °C for 2 h to yield a crystallized CBC/$MoSe_2$-1 hybrid. Meanwhile, CBC/$MoSe_2$-2 and CBC/$MoSe_2$-3 hybrids were also obtained with different Na_2MoO_4 quantities of 23.0 and 46 mg, and Se solution of 5 and 10 mL, respectively.

Synthesis of Template-Free $MoSe_2$ Aggregates: Template-free $MoSe_2$ aggregates were prepared via the same method as CBC/$MoSe_2$ hybrid, while the only difference was that no CBC nanofibers were added during the solvothermal process.

Characterization: Morphology of the samples was observed by FESEM (Ultra 55, Zeiss) at an acceleration voltage of 5 kV. The TEM, HR-TEM were carried out on a JEM-2100F field emission electron microscope at an acceleration voltage of 200 kV. XRD patterns were obtained on a Philips X'Pert Pro Super diffractometer with Cu Kα radiation (λ = 0.1542 nm). XPS were acquired on an ESCALAB MK II with Mg Kα as the excitation source.

Calculations: The first-principle calculations were carried out with the Vienna ab initio simulation package.[45] The projector augmented wave potentials are used to describe the interaction between ions and valence electrons, and the generalized gradient approximation in the Perdew–Burke–Ernzerhof form is used to treat the exchange-correlation between electrons.[46,47] To achieve the accurate density of electronic states, the one-electron wave functions in a plane-wave basis were expanded with an energy cutoff of 500 eV. In addition, the Gamma centered Monkhorst–Pack mesh is used to sample the Brillouin zone for all the structures with the k-point separation <0.07 $Å^{-1}$. Ionic relaxations were carried out under the conventional energy (10^{-5} eV) and force (0.01 eV $Å^{-1}$) convergence criteria. To study the mechanism of HER processes, the well-established climbing-image nudged elastic band (CI-NEB) approach was utilized.[48] The computational modeling of the HER processes was performed by periodic density functional theory with the Vienna ab initio Simulation Package.

Electrochemical Measurements: All of the electrochemical measurements were performed in a three-electrode system on an electrochemical workstation (CHI 660D, Shanghai Chenhua Instrument Co., China), where the electrochemical catalysts were used as the working electrodes, Pt wire as the counter electrode, and saturated calomel electrode ($Hg/HgCl_2$ in saturated KCl, SCE) as the reference electrode, respectively. Typically, 4 mg of electrochemical catalyst and 30 µL of Nafion solution (Sigma Aldrich, 5 wt%) were dispersed in 1 mL water–DMF solution by sonication for 30 min to form a homogeneous emulsion. After that, 5 µL of the emulsion was loaded onto a polished glassy carbon electrode (GCE) with 3 mm diameter. Linear sweep voltammetry was conducted in 0.5 M N_2-purged H_2SO_4 solution at room temperature with a scan rate of 5 mV s^{-1}. All the potentials reported in this

work were calibrated to RHE according to the equation of $E_{RHE} = E_{SCE} + (0.241 + 0.059\ pH)$ V. Tafel plots are derived from the polarization curves of various samples, which are fitted well with the Tafel equation of $\eta = b\ \log(j) + a$ (where η is the overpotential, j is the current density, and b is the Tafel slope). EIS measurements were conducted by applying an AC voltage in the frequency range between 100 kHz and 10 mHz with an amplitude of 5 mV.

Supporting Information

Supporting Information is available from the Wiley Online Library or from the author.

Acknowledgements

The authors are grateful for the financial support from the National Natural Science Foundation of China (51125011, 51373037, 51433001).

[1] M. S. Dresselhaus, I. L. Thomas, *Nature* **2001**, *414*, 332.
[2] J. A. Turner, *Science* **2004**, *305*, 972.
[3] M. G. Walter, E. L. Warren, J. R. Mckone, S. W. Boettcher, Q. Mi, E. A. Santori, N. S. Lewis, *Chem. Rev.* **2010**, *110*, 6446.
[4] J. K. Norskov, C. H. Christensen, *Science* **2006**, *312*, 1322.
[5] C. L. Tan, H. Zhang, *Chem. Soc. Rev.* **2015**, *44*, 2713.
[6] J. F. Xie, J. J. Zhang, S. Li, F. Grote, X. D. Zhang, H. Zhang, R. X. Wang, Y. Lei, B. C. Pan, Y. Xie, *J. Am. Chem. Soc.* **2013**, *135*, 17881.
[7] C. Kammerer, G. Prestat, D. Madec, G. Poli, *Acc. Chem. Res.* **2014**, *47*, 3439.
[8] X. L. Zhou, Y. Liu, H. X. Ju, B. C. Pan, J. F. Zhu, T. Ding, C. D. Wang, Q. Yang, *Chem. Mater.* **2016**, *28*, 1838.
[9] X. L. Zhou, J. Jiang, T. Ding, J. J. Zhang, B. C. Pan, J. Zuo, Q. Yang, *Nanoscale* **2014**, *6*, 11046.
[10] Q. H. Wang, K. Kalantar-Zadeh, A. Kis, J. N. Coleman, M. S. Strano, *Nat. Nanotechnol.* **2012**, *7*, 699.
[11] S. Balendhran, S. Walia, H. Nili, J. Z. Ou, S. Zhuiykov, R. B. Kaner, S. Sriram, M. Bhaskaran, K. Kalantar-zadeh, *Adv. Funct. Mater.* **2013**, *23*, 3952.
[12] Y. F. Shi, C. X. Hua, B. Li, X. P. Fang, C. H. Yao, Y. C. Zhang, Y. S. Hu, Z. X. Wang, L. Q. Chen, D. Y. Zhao, G. D. Stucky, *Adv. Funct. Mater.* **2013**, *23*, 1832.
[13] H. Tang, K. P. Dou, C. C. Kaun, Q. Kuang, S. H. Yang, *J. Mater. Chem. A* **2014**, *2*, 360.
[14] Y. Yan, B. Y. Xia, Z. C. Xu, X. Wang, *ACS Catal.* **2014**, *4*, 1693.
[15] J. F. Xie, H. Zhang, S. Li, R. X. Wang, X. Sun, M. Zhou, J. F. Zhou, X. W. Lou, Y. Xie, *Adv. Mater.* **2013**, *25*, 5807.
[16] X. Y. Yu, H. Hu, Y. W. Wang, H. Y. Chen, X. W. Lou, *Angew. Chem., Int. Ed.* **2015**, *54*, 7395.
[17] V. M. Agranovich, T. A. Leskova, *Prog. Surf. Sci.* **1988**, *29*, 169.
[18] F. C. Lei, Y. F. Sun, K. T. Liu, S. Gao, L. Liang, B. C. Pan, Y. Xie, *J. Am. Chem. Soc.* **2014**, *136*, 6826.
[19] X. Lei, K. Yu, H. L. Li, Z. Tang, Z. Q. Zhu, *J. Phys. Chem. C* **2016**, *120*, 15096.
[20] J. Rhyee, J. Kwon, P. Dak, J. H. Kim, S. M. Kim, J. Park, Y. K. Hong, W. G. Song, I. Omkaram, M. A. Alam, S. Kim, *Adv. Mater.* **2016**, *28*, 2316.
[21] G. Cunningham, M. Lotya, C. S. Cucinotta, S. Sanvito, S. D. Bergin, R. Menzel, M. S. P. Shaffer, J. N. Coleman, *ACS Nano* **2012**, *6*, 3468.
[22] X. L. Hu, W. Zhang, X. X. Liu, Y. N. Mei, Y. H. Huang, *Chem. Soc. Rev.* **2015**, *44*, 2376.
[23] F. H. Saadi, A. I. Carim, J. M. Velazquez, J. H. Baricuatro, C. C. L. McCrory, M. P. Soriaga, N. S. Lewis, *ACS Catal.* **2014**, *4*, 2866.
[24] Z. Y. Lei, S. J. Xu, P. Y. Wu, *Phys. Chem. Chem. Phys.* **2016**, *18*, 70.
[25] S. Tongay, J. Zhou, C. Ataca, K. Lo, T. S. Matthews, J. B. Li, J. C. Grossman, J. Q. Wu, *Nano Lett.* **2012**, *12*, 5576.
[26] Y. P. Huang, H. Y. Lu, H. H. Gu, J. Fu, S. Y. Mo, C. Wei, Y. E. Miao, T. X. Liu, *Nanoscale* **2015**, *7*, 18595.
[27] F. L. Lai, Y. P. Huang, L. Z. Zuo, H. H. Gu, Y. E. Miao, T. X. Liu, *J. Mater. Chem. A* **2016**, *4*, 15861.
[28] Z. Y. Wu, H. W. Liang, L. F. Chen, B. C. Hu, S. H. Yu, *Acc. Chem. Res.* **2016**, *49*, 96.
[29] F. L. Lai, Y. E. Miao, Y. P. Huang, Y. F. Zhang, T. X. Liu, *ACS Appl. Mater. Interfaces* **2016**, *8*, 3558.
[30] C. T. Chen, Y. Huang, C. L. Zhu, Y. Nie, J. Z. Yang, D. P. Sun, *Chin. J. Polym. Sci.* **2014**, *32*, 439.
[31] X. Guo, G. L. Cao, F. Ding, X. Y. Li, S. Y. Zhen, Y. F. Xue, Y. M. Yan, T. Liu, K. N. Sun, *J. Mater. Chem. A* **2015**, *3*, 5041.
[32] F. L. Lai, Y. E. Miao, L. Z. Zuo, H. Y. Lu, Y. P. Huang, T. X. Liu, *Small* **2016**, *12*, 3235.
[33] H. Wang, X. Y. Wang, L. Wang, J. Wang, D. L. Jiang, G. P. Li, Y. Zhang, H. H. Zhong, Y. Jiang, *J. Phys. Chem. C* **2015**, *119*, 10197.
[34] A. Y. S. Eng, A. Ambrosi, Z. Sofer, P. Simek, M. Pumera, *ACS Nano* **2014**, *8*, 12185.
[35] S. J. Xu, Z. Y. Lei, P. Y. Wu, *J. Mater. Chem. A* **2015**, *3*, 16337.
[36] L. Yang, Q. Fu, W. H. Wang, J. Huang, J. L. Huang, J. Y. Zhang, B. Xiang, *Nanoscale* **2015**, *7*, 10490.
[37] Y. P. Huang, Y. E Miao, J. Fu, S. Y. Mo, C. Wei, T. X. Liu, *J. Mater. Chem. A* **2015**, *3*, 16263.
[38] S. Mao, Z. H. Wen, S. Q. Ci, X. R. Guo, K. K. Ostrikov, J. H. Chen, *Small* **2015**, *11*, 414.
[39] Y. J. Zhang, Q. F. Gong, L. Li, H. C. Yang, Y. G. Li, Q. B. Wang, *Nano Res.* **2015**, *8*, 1108.
[40] Z. Q. Liu, N. Li, H. Y. Zhao, Y. P. Du, *J. Mater. Chem. A* **2015**, *3*, 19706.
[41] Y. D. Liu, L. Ren, Z. Zhang, X. Qi, H. X. Li, J. X. Zhong, *Sci. Rep.* **2016**, *6*, 22516.
[42] Y. Zheng, Y. Jiao, M. Jaroniec, S. Z. Qiao, *Angew. Chem., Int. Ed.* **2015**, *54*, 52.
[43] Y. R. Zheng, M. R. Gao, Z. Y. Yu, Q. Gao, H. L. Gao, S. H. Yu, *Chem. Sci.* **2015**, *6*, 4594.
[44] F. L. Lai, Y. E. Miao, L. Z. Zuo, Y. F. Zhang, T. X. Liu, *ChemNanoMat* **2016**, *2*, 212.
[45] G. Kresse, J. Furthmuller, *Phys. Rev. B* **1996**, *54*, 11169.
[46] J. P. Perdew, K. Burke, M. Ernzerhof, *Phys. Rev. Lett.* **1996**, *77*, 3865.
[47] J. F. Xie, S. Li, X. D. Zhang, J. J. Zhang, R. X. Wang, H. Zhang, B. C. Pan, Y. Xie, *Chem. Sci.* **2014**, *5*, 4615.
[48] G. Henkelman, B. P. Uberuaga, H. Jonsson, *J. Chem. Phys.* **2000**, *113*, 9901.

Received: August 27, 2016
Revised: October 22, 2016
Published online: December 5, 2016

